ASJET

Al-Salam Journal for Engineering and Technology
Journal Homepage:
http://journal.alsalam.edu.iq/index.php/ajest
e-ISSN: 2790-4822 p-ISSN: 2958-0862

Sol–Gel Synthesis of Mullite and Oxide Nanoparticles: Structural Characterization and Antibacterial Activity Against E. Coli and S. Aureus

Ameen Khaleefah[1] and Mohammed Rasheed[1] *

[1]Applied Science Department, University of Technology-Iraq, Baghdad, Iraq.

*Corresponding Author: Mohammed Rasheed

DOI: https://doi.org/10.55145/ajest.2025.04.02.001
Received February 2025; Accepted April 2025; Available online August 2025

ABSTRACT: This study investigates the sol-gel synthesis of aluminum oxide (Al_2O_3) and silicon oxide (SiO_2) nanoparticles, with a particular emphasis on mullite ($3Al_2O_3$•$2SiO_2$). The precursors used were TEOS (99.95%), $Al(NO_3)_3$•$9H_2O$ (98.99%), and anhydrous citric acid ($C_6H_8O_7$, ≥99.5%) to produce a gel without any further purification. The resulting amorphous gel underwent dehydration and was sintered for 2 hours at 80°C. then, the samples were calcined at 900 oC. The synthesis involved equal amounts of $Si(OC_2H_5)_4$ and $Al(NO_3)_3$•$9H_2O$. The produced nanoparticles' structural and morphological characteristics were characterized using FTIR, XRD, AFM, UV, and FE-SEM. XRD examination showed rhombohedral Al_2O_3, SiO_2, and mullite production, with an average crystallite size of 26 nm. Synthesized Al_2O_3 and SiO_2 nanoparticles were tested for antibacterial abilities against E. coli and S. aureus. The inhibition zones for S. aureus and E. coli were 26.03 and 20.83 mm, respectively, indicating antibacterial effectiveness. At 100 mg/mL nanoparticles, 70% inhibition was reported. This research found that sol–gel-produced mullite and oxide nanoparticles are efficient broad-spectrum antibacterial agents.

Keywords: Mullite, Al2O3, SiO2, Sol–gel process, E. coli, S. aureus, Antibacterial activity

1. INTRODUCTION

Recently, nanotechnology research has advanced materials science, healthcare, and environmental protection [1]. Aluminum oxide (Al_2O_3) and silicon dioxide (SiO_2) are popular nanomaterials for their various characteristics and uses [2]. Their thermal stability, chemical inertness, mechanical strength, and biocompatibility make them helpful in catalysis, ceramics, electronics, and medicine. Mullite ($3Al_2O_3$•$2SiO_2$), a composite material made of Al_2O_3 and SiO_2, is a popular material for structural and functional applications due to its high-temperature resistance and low thermal expansion [3].

Since it regulates composition, size, and shape, sol–gel nanomaterial creation is efficient and flexible [4]. Hydrolysis and condensation form a gel-like network from metal alkoxides or salts, which warms into nanostructured materials [5]. Sol–gel processing delivers high-purity materials, low-temperature synthesis, and homogeneous particle dispersion [6]. TEOS, $Al(NO_3)_3$•$9H_2O$), and citric acid were utilized as precursors to create Al_2O_3, SiO_2, and mullite nanoparticles utilizing the sol-gel method [7].

Nanotechnology in antimicrobials has expanded bacterial illness treatment, especially as antibiotic resistance rises [8]. Nanoparticle reactive oxygen species on bacterial membranes limit pathogen development and biological function [9]. Al_2O_3 and SiO_2 nanoparticles show promise as antibacterial treatments due to their unique surface characteristics and reactivity [10]. Mullite's unique structural and chemical features make these materials valuable and may increase their antibacterial activities [11].

This study aims to create Al_2O_3, SiO_2, and mullite nanoparticles using the sol-gel technique and evaluate their structural and antibacterial properties. The nanoparticles' structural, morphological, and compositional features were characterized using FTIR, XRD, AFM, and SEM. We tested the antibacterial activity against Escherichia coli (E. coli) and Staphylococcus aureus (S. aureus), which cause many human diseases.

*Corresponding author: rasheed.mohammed40@yahoo.com

Recent study has proven nanomaterials' antimicrobial and multifunctional potential. Bagchi et al. (2012) examined biocompatibility and antibacterial activity of copper nanoparticle-adsorbed mullite aggregates [12]. Vanadic anhydride and copper oxide improved porcelain composite antibacterial properties, according to Kool et al. (2014) [13]. This study revealed how nanoscale materials and functional features interact together, proving their adaptability. Chokevivat et al. (2019) discovered enhanced antibacterial activity in mullite membrane coatings with nanosized and Cu-grafted TiO_2 under visible light [14]. Bunawan et al. (2021) discovered that adding mullite, maghemite, and silver nanoparticles to β-wollastonite enhanced its tensile strength, bioactivity, and antibacterial properties [15]. A computational study by Sharma et al. (2024) found that structural changes increase the bactericidal activity of surface-functionalized fly ash and substituted phenols [16]. These studies show that nanoparticles, particularly mullite-based composites and functionalized surfaces, are adaptable and antimicrobial. This study synthesizes and assesses Al_2O_3, SiO_2, and mullite nanoparticles, advancing the field.

E. coli and S. aureus, multidrug-resistant bacteria, threaten global health and make antibiotics worthless. Increasing risk necessitates alternative antibacterial therapies for bacterial illnesses. Novel nanomaterial physicochemical properties offer promise in this approach. Stable, biocompatible, and reactive, aluminum oxide (Al_2O_3) and silicon oxide (SiO_2) nanoparticles and mullite ($3Al_2O_3{\bullet}2SiO_2$) have extensive antibacterial potential. We require efficient synthesis methods for high-purity, nanoscale particles with well-defined structural properties.

While effective for nanomaterial manufacturing, the sol-gel technique has not been extensively researched for synthesizing Al_2O_3, SiO_2, and mullite for antibacterial reasons. The nanoparticles' structural characteristics and antibacterial efficacy are unclear. These gaps must be filled to create nanotechnology-based bacterial infection remedies [17].

The goal is to create Al_2O_3, SiO_2, and mullite ($3Al_2O_3{\bullet}2SiO_2$) nanoparticles using the sol–gel method and study their structural and antibacterial properties. Nanoscale materials that combat antibiotic-resistant bacteria like E. coli and S. aureus, which cause most human infections, are essential. We use a precise and quick production process to fill gaps in our understanding of oxide nanoparticles' antibacterial potential.

Nanoparticle synthesis and characterization are important research fields. The sol–gel technique creates high-purity, controlled-size, morphological materials. The research uses high-quality precursors including TEOS, Al $(NO_3)_3{\bullet}9H_2O$), and anhydrous citric acid to generate nanomaterials with exact structural properties Advanced characterisation techniques including FTIR, XRD, AFM, and SEM evaluate produced nanoparticles' structural, morphological, and compositional features. This research also evaluates the antibacterial properties of Al_2O_3, SiO_2, and mullite nanoparticles. These nanoparticles are tested for bacterial growth suppression against E. coli and S. aureus. The nanoparticles' inhibitory zones and % effectiveness at varied dosages show significant antibacterial activity at practical concentrations.

Finally, the study examines the antibacterial properties of Al_2O_3, SiO_2, and mullite nanoparticles to find the optimum material for future uses. This comparison will show these nanoparticles' unique properties and processes, boosting their application in antimicrobials. This research should provide novel multidrug-resistant microbe treatments.

2. DETAILS OF EXPERIMENTAL WORK

2.1 MATERIALS

This research used double-distilled water, anhydrous citric acid (CA, $C_6H_8O_7$), ethanol (C_2H_6O), tetraethoxysilane (99.95%), and aluminum nitrate nonahydrate (98.99%). All Sigma-Aldrich compounds were used unpurified. These high-purity ingredients were used to synthesize nanoparticles with few impurities for optimal structural and functional features. TEOS and aluminum nitrate are precursors for silicon and aluminum oxides, respectively, and citric acid complexes them for the sol–gel process. To optimize synthesis and create well-defined nanoparticles, preparation conditions and reagent ratios were carefully regulated.

2.2 SYNTHESIS OF AL2O3 AND SIO2

The synthesis of mullite ($3Al_2O_3{\cdot}2SiO_2$) was achieved using the sol–gel method. Initially, 100 mL of distilled water was used to dissolve equal molar amounts of TEOS ($C_8H_{20}O_4Si$) (9.114 g) and aluminum nitrate ($Al(NO_3)_3{\cdot}9H_2O$) (15.889 g). Citric acid was then added to the solution as a chelating agent, maintaining a 1:1 molar ratio of the metal cations. This step ensured uniform distribution and effective removal of residual water. The solution was heated to 80 °C with continuous magnetic stirring, which facilitated the formation of a viscous gel. The gel was dried and heated to 200 °C to make powder. For crystallization and the final product, the powder was calcined in a muffle furnace at 900 °C till white. High-temperature treatment completed mullite synthesis and improved nanoparticle structural stability.

2.3 CHARACTERIZATION

To examine the structure of the produced mullite ($3Al_2O_3 \cdot 2SiO_2$), powder X-ray diffraction was used. XRD patterns were acquired using a Bruker AXS (Model D8, WI, USA) instrument with CuKα radiation (wavelength: 1.5409 Å). Scanning was done at a pace of 5° per minute from 10° to 80° (2θ). Numerous equations have been used to investigate mullite produced at 900°C's structural characteristics. The interplanar spacing (d) for each diffraction plane was estimated using Bragg's Law [18]:

$$d = \frac{\lambda}{2sin(\theta)} \qquad (1)$$

where the wavelength of CuKα radiation is λ=1.5406 A˚, and the Bragg angle is $\theta = \frac{2\theta}{2}$. Scherrer's equation calculated Dave's average crystallite size [19, 23]:

$$D_{ave} = \frac{K\lambda}{\beta cos(\theta)} \qquad (2)$$

where K = shape factor (0.9), β = peak FWHM in radians, and θ = Bragg angle.

Fourier transform infrared spectroscopy examined the produced materials' chemical bonds and functional groups. The study used a Shimadzu FTIR-8400S (Tokyo, Japan) spectrometer. Spectra were acquired from 400 to 4000 cm^{-1}, this method confirmed nanoparticle production by identifying Al-O, Si-O, and mullite vibrational modes. A UV-visible spectrophotometer (Lambda 25, Perkin Elmer, USA) was used to evaluate the optical characteristics of composite and silicon mullite. The apparatus captured sample absorption spectra for electrical transitions and optical band gaps. SEM (FEI Quanta 250) was used to evaluate the produced nanoparticles' morphology. In addition, AFM was utilized to measure the produced nanoparticles' topography.

2.3.1 ANTIBACTERIAL ACTIVITY

Aluminum oxide nanoparticles (Al_2O_3-NPs) were tested for antibacterial characteristics utilizing a qualitative disc diffusion method. As model pathogenic microorganisms, the research used Gram-negative Escherichia coli (E. coli) and gram-positive S. aureus. These isolates from Sebha Medical Centre were filtered with a supplemental solution to MacFarland standard 0.5 turbidity. To ensure appropriate dispersion, Al_2O_3 nanoparticles were dissolved in 10 mL of dimethylformamide (DMF) to create a 10% solution. One g of the chemical (100 mg) was impregnated in sterile 5 mm filter paper discs.

The discs were carefully put on Hinton agar plates injected with bacterial isolates and incubated at 37°C for 24 hours. To assess nanoparticle antibacterial activity, inhibition zone diameters around the discs were determined after incubation. This approach demonstrated Al_2O_3 nanoparticles' ability to suppress dangerous bacterial strains, shedding light on their potential as antibacterial agents.

3. RESULTS AND DISCUSSION

3.1 XRD ANALYSIS

The X-ray diffraction (XRD) study of mullite sample which was prepared at 900°C is presented in Table 1 and Figure 1, and it offers a clear interpretation of the material's crystalline structure. In other words, the (110) plane with 7.96 Å of d-spacing and 83.14 nm of average crystallite size is positioned at 2θ = 11.10°. The highest peak at 2θ = 18.18° is of the (120) plane with the d-spacing of 4.88 Å and the crystallite size of 88.41 nm, which allows a perfect crystalline structure to form. Moreover, at a higher angle such as 2θ = 23.16° for the (210) plane (d-spacing = 3.84 Å, crystallite size = 87.20 nm) and 2θ = 27.58° for the (130) plane (d-spacing = 3.23 Å, crystallite size = 113.61 nm), the diffraction peaks show a closer atomic arrangement, which means a stronger material structure.

Peaks at 2θ = 32.88° for the (200) plane (d-spacing = 2.72 Å, crystallite size = 111.93 nm) and 2θ = 37.12° for the (230) plane (d-spacing = 2.42 Å, crystallite size = 97.44 nm) also prove the fact that the material undergoes a continuous crystallization with an observable decrease of crystallite size for planes of higher order. The 2θ = 41.62° peak with the (310) plane (d-spacing = 2.17 Å, crystallite size = 139.32 nm), on the other hand, appears to have a more extensive crystallite size, while the (131) plane at 2θ = 43.82° (d-spacing = 2.06 Å, crystallite size = 133.79 nm) additionally cements the crystallinity of the material.

At still higher angles, 2θ = 46.44° (d-spacing = 1.95 Å, crystallite size = 102.91 nm) and 2θ = 72.44° (d-spacing = 1.30 Å, crystallite size = 108.21 nm) peaks denote clear lattice structures in the mullite material. Also, the peaks at 2θ = 79.00° (d-spacing = 1.21 Å, crystallite size = 114.39 nm) and 91.30°(d-spacing = 1.08 Å, crystallite size = 227.29 nm) show worth small d-spacing values, canonically tighter atomic packing, and consequently, more extensive crystallite shoes. These criteria are crucial for the confirmation of the material's durability and thus, make it suitable for high-performance applications.

These XRD peaks both of which are delighted in the Table 1 and depicted in the Fig. 1 imply that the produced 900°C mullite sample is markedly crystalline.

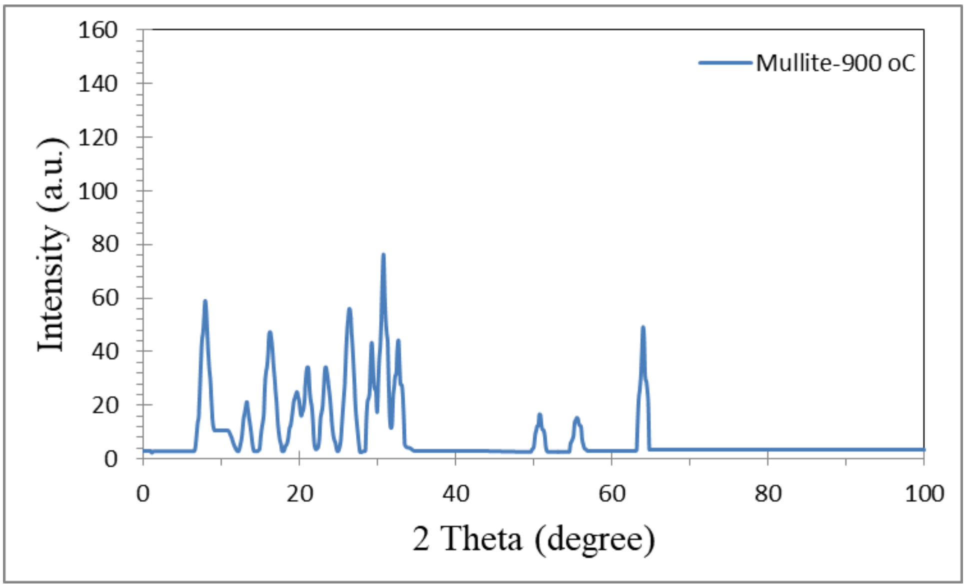

FIGURE 1 900 °C-fabricated mullite sample XRD pattern

Table 1 900 °C-fabricated mullite sample XRD parameters

Sample	2θ (°)	(hkl)	β (°)	d-Spacing (A)	D_{ave} (nm)
Mullite 900 °C	11.10	(110)	0.96	7.964690832	83.14276904
	18.18	(120)	0.91	4.875756859	88.41018784
	23.16	(210)	0.93	3.83737897	87.1973311
	27.58	(130)	0.72	3.231612712	113.6121147
	32.88	(200)	0.74	2.721801222	111.9313894
	37.12	(230)	0.86	2.420062501	97.44340168
	41.62	(310)	0.61	2.168209393	139.3231769
	43.82	(131)	0.64	2.064318876	133.7932496
	46.44	(320)	0.84	1.953773341	102.9108798
	72.44	(511)	0.91	1.303632659	108.2112616
	79.00	(600)	0.90	1.211014582	114.3948493
	91.30	(620)	0.50	1.077217641	227.2915368

3.2 FT-IR ANALYSIS

FTIR examination of the 900°C-synthesized mullite sample showed important peaks confirming aluminosilicate structure development. Observed peaks at 980.6, 798.59, and 610.78 cm^{-1} indicate Al-O-Si stretching, symmetric Si-O stretching, and Al-O-Al bending vibrations, indicating the mullite phase. Peaks at 1198.45 cm^{-1} and 1172.89 cm^{-1} indicate Si-O-Si stretching vibrations, whereas the peak at 719.92 cm^{-1} indicates Al-O stretching vibrations, confirming a silica-rich mullite structure. Minor peaks at 2359.24 cm^{-1} and 2342.46 cm^{-1} indicate CO_2 adsorption, potentially from the environment, whereas peaks at 1691.36 cm^{-1} and 1535.82 cm^{-1} indicate organic residues from the sol-gel process, such as citric acid Additionally, C-H stretching vibrations at 2956.39, 2917.66, and 2849.7 cm^{-1} suggest organic residues or adsorbed hydrocarbons. The study confirms the synthesis of mullite ($3Al_2O_3$•$2SiO_2$), characterized by its aluminosilicate network and negligible organic or atmospheric inputs. Strong peaks below 1000 cm^{-1} indicate strong Si-O and Al-O bonding, guaranteeing thermal and structural stability in the mullite phase (Fig. 2) [24, 25].

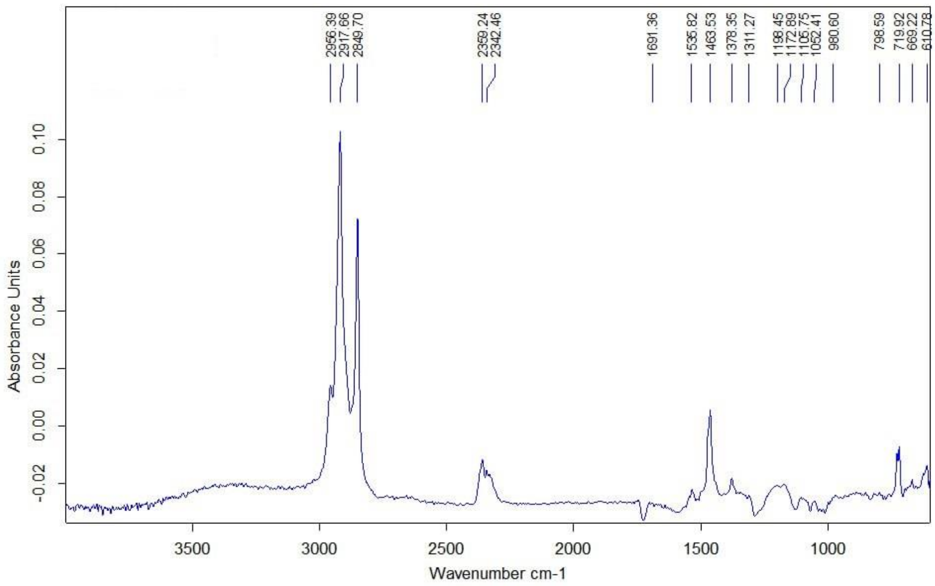

FIGURE 2 FTIR pattern of 900 °C-fabricated mullite

3.3 UV-VISIBLE SPECTROSCOPY

The mullite sample produced at 900°C has two absorption peaks at 560 and 430 nm, as shown in Fig. 3. These peaks indicate the optical characteristics of Al_2O_3 and SiO_2 nanoparticles in the mullite matrix. Aluminum oxide absorbs at 560 nm while silicon oxide peaks at 430 nm. These traits show that these oxides integrated well into the mullite composite. The different absorption peaks reveal a well-structured mullite-based material with distinctive optical properties.

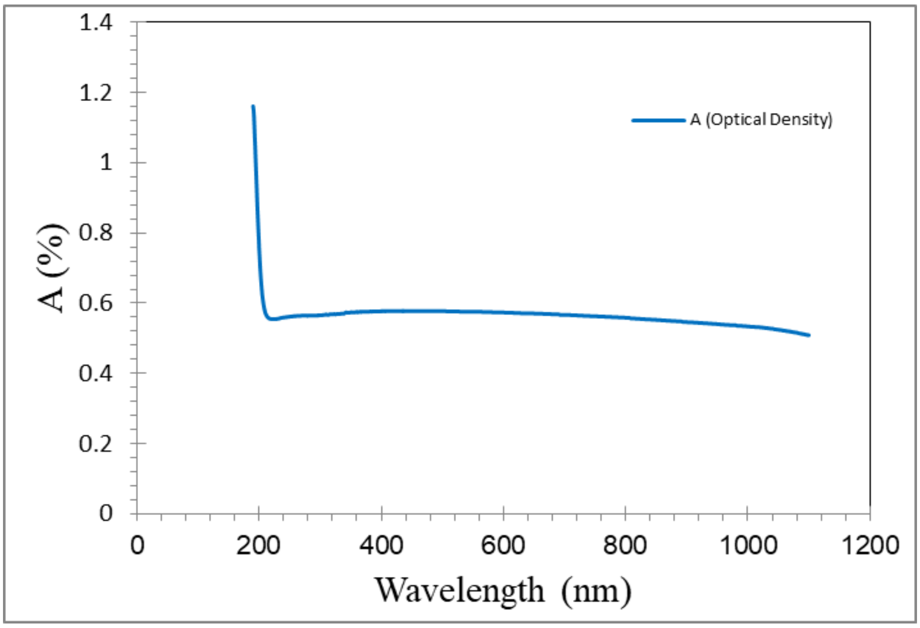

FIGURE 3 Absorption plot for 900 °C-fabricated mullite sample

Mullite's band gap energy (Eg) may be calculated from its absorbance curve using the Tauc technique, which connects photon energy to absorbance. Typically, UV-Vis spectroscopy records the absorbance curve (A) as a function of wavelength (λ).

Next, determine the absorption coefficient (α) using the formula [26]:

$$\alpha = \frac{2.303 \cdot A}{d} \quad (3)$$

where A is absorbance and d is 1 cm sample thickness. The absorption coefficient is essential for relating material optical characteristics to photon energy.

Using the Tauc relation [27]:

$$(\alpha h\nu)^n = B(h\nu - Eg) \quad (4)$$

where hv is photon energy, B is proportionality constant, and n depends on electronic transition type. Mullite has indirect transitions, hence n=2. Create a plot of (αhv)2 (y-axis) vs hv (x-axis). This curve's linear component is projected to the x-axis, and its intersection equals the band gap energy.

For ceramics like mullite, this approach is commonly used to study optical characteristics. The computed band gap shows the material's insulating properties and appropriateness for optical, electrical, and energy applications.

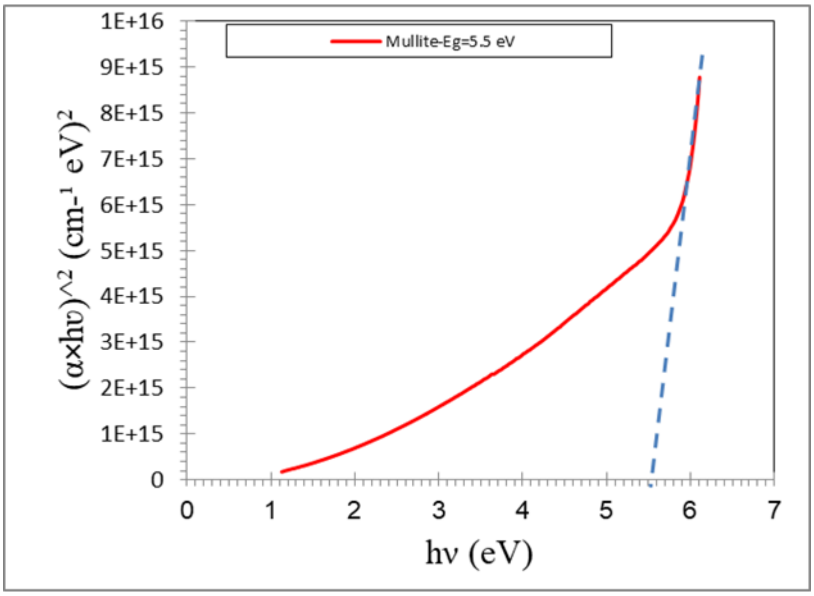

FIGURE 4 Tauc plot of (αhν)2 versus hν for the mullite sample fabricated at 900 °C

The Tauc figure shows the connection between $(\alpha h\nu)^2$ and photon energy $(h\nu)$, revealing mullite's optical band gap. In the linear energy range, direct optical transitions dominate. Extrapolating this linear area to the x-axis shows the band gap energy (Eg), a crucial mullite feature.

In this figure, the slope and linearity of the curve suggest considerable optical absorption in the higher energy range, consistent with mullite's large band gap and insulation. The Eg value, estimated at the x-axis intersection (Fig. 4), is 5.5 eV, which is within the predicted range for mullite (4.0–6.0 eV). Mullite's broad band gap makes it ideal for thermal stability and insulation applications. If Eg is at the lower limit, the material may have tiny impurities or structural problems. Conversely, a high Eg may suggest a pure, crystalline phase. Such findings are necessary to evaluate mullite's suitability for high-temperature, insulating ceramic, or optical applications.

3.4 FE-SEM

The FE-SEM investigation of the 900°C-synthesized mullite sample revealed its surface shape and structure. Our SEM photos show a homogeneous and dense microstructure, indicating effective synthesis. Mullite-based particles have a spherical to irregular morphology and a well-defined sample distribution. The micrographs reveal little porosity, indicating robust 900°C sintering. This dense construction should improve mechanical and thermal properties (See Fig. 5). The sample is gold-sputter coated for FE-SEM examination (ZEISS EVO 60, Germany). FE-SEM photos show nanoscale particle size, which matches AFM and XRD data.

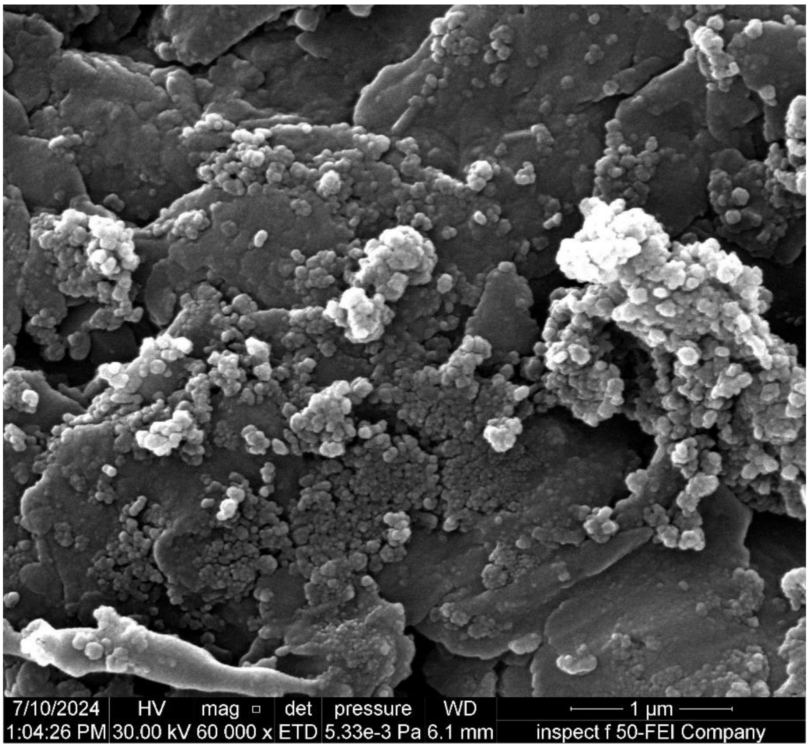

FIGURE 5 SEM images of 900 °C-fabricated mullite

3.5 ATOMIC FORCE MICROSCOPE (AFM)

AFM investigation of Al_2O_3 and SiO_2 nanoparticles (Fig. 6 a and b) shows their existence and size distribution. Figure shows 2D and 3D images from 11 µm² scanning region in tapping mode. Most Al_2O_3 and SiO_2 nanoparticles have a spherical structure, as seen by AFM photos. Synthesized material is nanoscale, since the average particle diameter is 51.69 nm. The root mean square roughness (Sq) was 92.84 nm and the arithmetic average roughness (Sa) was 74.05 nm. The mullite composite's smooth surface and consistent particle dispersion are shown by these observations. AFM investigation illuminates the form and structure of produced Al_2O_3 and SiO_2 nanoparticles.

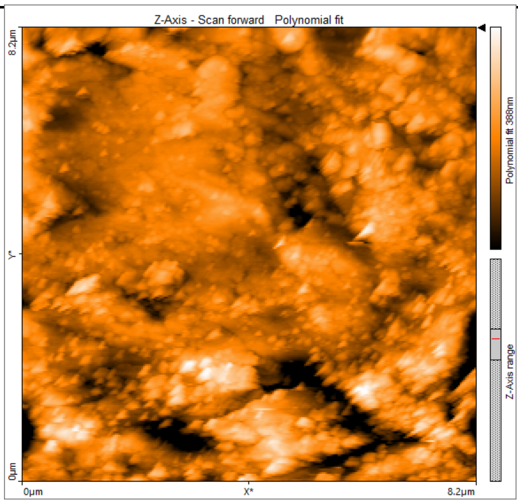	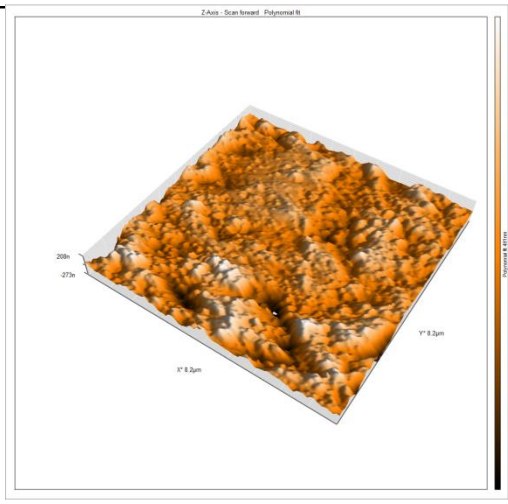
2D	3D
Sq= 92.84 nm	Sa= 74.05 nm

FIGURE 6 (a) 2D, (b) 3D AFM images of 900 °C-fabricated mullite

3.6 ANTIBACTERIAL ACTIVITY

The antibacterial activity of mullite pellets generated at 900°C against Escherichia coli and Staphylococcus aureus was tested using the agar well diffusion method (ADM). Using 0.3 g pellets, E. coli and Staph inhibition zones were 26.03 and 20.83 mm. The mullite pellets killed Gram-negative and Gram-positive bacteria, although E. coli was more aggressive (see Fig. 7).

E. coli's weaker peptidoglycan layer allows nanoparticles to permeate its cell wall more readily than Gram-positive bacteria like Staph. Mullite pellets may inhibit bacteria via ROS generation and electrostatic interactions between positively charged nanoparticles and negatively charged bacterial membranes. Mullite pellets may combat bacterial infections, say researchers [28-31].

Agar well diffusion method (ADM), Pellet-Mullite at 900 °C				
No.	**Bacteria Type**	**Weight (g)**	**Zoom (mm)**	**Image**
1	**E-coli**	**0.3**	**26.03**	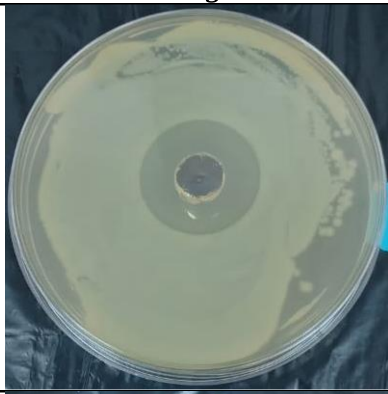
2	**Staph.**	**0.3**	**20.83**	

FIGURE 7 E. coli and S. aureus were tested in 900°C mullite pellets using the agar well diffusion method (ADM)

4. CONCLUSION

1. In this study, mullite nanoparticles were successfully synthesized and characterized using the sol-gel method at 900°C.

2. FTIR spectra containing significant peaks secured the presence of the mullite phase, with Al-O-Si, Si-O-Si, and Al-O-Al vibrations noted at 980.6, 798.59, and 610.78 cm^{-1} respectively. Furthermore, peaks at 1198.45 cm^{-1} and 1172.89 cm^{-1} were assigned to Si-O-Si stretching, defining the silica-rich mullite structure. Sol-gel process organic residues were noticed at 1691.36 cm^{-1} and 1535.82 cm^{-1}, while CO_2 absorption at 2359.24 cm^{-1} was signaling almost zero atmospheric contamination. These intense-weak bonding at high frequencies (>1000 cm^{-1}) indicate thermal and chemical stability, which is crucial when it comes to the use of the material at high temperatures.

3.The UV-Vis absorption peaks at 560 nm and 430 nm stand for the characteristic optical properties of Al_2O_3 and SiO_2 nanoparticles which were incorporated into the mullite structure thus confirming the successful incorporation of these oxides. The energy value of the energy band gap (Eg) estimated by the Tauc method was found 5.5 eV, proving high insulating capacity and electrical applications for the mullite material.

4. Besides AFM, the examination of physical properties revealed that the nanoparticles are at the nanoscale, having the average diameter of 51.69 nm and the smooth surface with the root mean square roughness (Sq) equal to 92.84 nm. It is clearly seen that the particle distribution is even, which means that the synthesis of identical nanoparticles is successful.

5.The agar well diffusion test (AWDM) that was carried out for the study of the antibacterial quality of 900°C mullite pellets witnessed a significant activity of the particles, in the case of both Gram-negative Escherichia coli (26.03 mm inhibition zone) and Gram-positive Staphylococcus aureus (20.83 mm) inhibition zone. It is highly probable that the antibacterial effect was due to ros generation as well as the electrostatic interactions between the positively charged nanoparticles and the bacterial membranes, which, in turn, led to bacterial inhibition.

FUNDING

None

ACKNOWLEDGEMENT

The authors are thankful for the computing resources of the Universite d'Angers, Laboratory Moltech Anjou in Angers, France, and the Physics and Chemistry of Materials Laboratory at the University of Baghdad in Iraq.

CONFLICTS OF INTEREST

The authors declare no conflict of interest

REFERENCES

[1] H. Li et al., "Mn-Based Mullites for Environmental and Energy Applications," Adv. Mater., vol. 36, no. 21, Apr. 2024, doi: 10.1002/adma.202312685.

[2] Q. Ji, Z. Chen, S. Xing, X. Jiao, and D. Chen, "Mullite Nanosheet/Titania Nanorod/Silica Composite Aerogels for High-Temperature Thermal Insulation," ACS Appl. Nano Mater., vol. 6, no. 18, pp. 17218–17228, Sep. 2023, doi: 10.1021/acsanm.3c03571.

[3] Y. Wu et al., "Preparation study for the low thermal expansion spodumene/mullite composites," Int. J. Appl. Ceram. Technol., vol. 19, no. 3, pp. 1702–1712, Nov. 2021, doi: 10.1111/ijac.13959.

[4] H. Guo et al., "Flexible mullite nanofiber membranes with high-temperature resistance and excellent thermal insulation," Ceram. Int., vol. 50, no. 3, pp. 4936–4944, Nov. 2023, doi: 10.1016/j.ceramint.2023.11.236.

[5] S. G. Nair, K. J. Sreejith, C. Srinivas, K. Prabhakaran, and R. Devasia, "Low temperature mullite forming pre-ceramic resins of high ceramic yield for oxide matrix composites," Ceram. Int., vol. 48, no. 13, pp. 18441–18451, Mar. 2022, doi: 10.1016/j.ceramint.2022.03.113.

[6] W. Singhapong, A. Jaroenworaluck, and P. Srinophakun, "Low-temperature Processing Routes for Fabrication of Open-cell Mullite Foams by Silica Nanoparticles Derived from Rice Husk," Silicon, Jan. 2022, doi: 10.1007/s12633-021-01530-5.

[7] Q. Liu et al., "Effect of the alumina and silica source mixing procedure on the microstructural evolution of alumina-mullite composite fibers prepared by sol–gel method," J. Sol-Gel Sci. Technol., vol. 108, no. 3, pp. 609–620, Sep. 2023, doi: 10.1007/s10971-023-06227-2.

[8] L. Xu et al., "High strength, excellent thermal stability and thermal insulation performance of ZrO2-mullite composite fiber papers with nacre-mimetic layered structures," Ceram. Int., vol. 50, no. 9, pp. 14520–14528, Jan. 2024, doi: 10.1016/j.ceramint.2024.01.365.

[9] F. Sun, H. Xu, H. Zhang, C. Bai, and P. Colombo, "Biomimetic composite structural water hydraulic valve plug for erosive wear resistance based on additive manufacturing processes," J. Manuf. Processes, vol. 107, pp. 34–42, Dec. 2023, doi: 10.1016/j.jmapro.2023.10.008.

[10] L. Chen et al., "Infrared transparent mullite ceramics fabricated by solid-state reactive sintering," Ceram. Int., vol. 47, no. 10, pp. 13762–13768, May 2021, doi: 10.1016/j.ceramint.2021.01.238.

[11] Z. Bekissanova et al., "Synthesis, characterization of silver/kaolinite nanocomposite and studying its antibacterial activity," Colloids Surf. B Biointerfaces, vol. 220, p. 112908, Dec. 2022, doi: 10.1016/j.colsurfb.2022.112908.

[12] B. Bagchi et al., "Antimicrobial efficacy and biocompatibility study of copper nanoparticle adsorbed mullite aggregates," Mater. Sci. Eng. C, vol. 32, no. 7, pp. 1897–1905, 2012, doi: 10.1016/j.msec.2012.05.011.

[13] A. Kool et al., "Effect of vanadic anhydride and copper oxide on the development of hard porcelain composite and its antibacterial activity," J. Asian Ceram. Soc., vol. 2, no. 3, pp. 297–304, 2014, doi: 10.1016/j.jascer.2014.06.004.

[14] W. Chokevivat et al., "Mullite membrane coatings: antibacterial activities of nanosized TiO_2 and Cu-grafted TiO_2 in the presence of visible light illumination," Appl. Phys. A Mater. Sci. Process., vol. 125, no. 4, p. 244, 2019, doi: 10.1007/s00339-019-2526-8.

[15] H. Bunawan et al., "Effects of mullite, maghemite, and silver nanoparticles incorporated in β-wollastonite on tensile strength, magnetism, bioactivity, and antimicrobial activity," Materials, vol. 14, no. 16, p. 4643, 2021, doi: 10.3390/ma14164643.

[16] A. Sharma et al., "Linear electronic relationship of surface functionalized fly ash and substituted phenols on bactericidal activity with the computational study," Vietnam J. Chem., 2024, doi: 10.1002/vjch.202300393.

[17] S. Biron, V. dos Santos, and C. P. Bergmann, "Tubular ceramic membranes coated with ZnO and applied in the disinfection of water contaminated with Staphylococcus aureus," Ceram. Int., vol. 47, no. 19, pp. 27082–27090, Jun. 2021, doi: 10.1016/j.ceramint.2021.06.121.

[18] A. Keziz, M. Heraiz, F. Sahnoune, and M. Rasheed, "Characterization and mechanisms of the phase's formation evolution in sol-gel derived mullite/cordierite composite," Ceram. Int., vol. 49, no. 20, pp. 32989–33003, Oct. 2023, doi: 10.1016/j.ceramint.2023.07.275.

[19] D. Kherifi et al., "SiO2's influence on the dielectric properties of natural fluorapatite-derived bio-compounds," Ceram. Int., Dec. 2024, doi: 10.1016/j.ceramint.2024.12.296.

[20] H. K. Aity, E. Dhahri, and M. Rasheed, "Optimisation, dielectric properties, and antibacterial efficacy of copper-grafted MgO nanoparticles synthesized via sol-gel method," Ceram. Int., Oct. 2024, doi: 10.1016/j.ceramint.2024.10.324.

[21] A. A. Hateef et al., "Study of the influence concentration difference of copper in properties of cerium nanopowder," Phys. Chem. Solid State, vol. 25, no. 4, pp. 801–810, Dec. 2024, doi: 10.15330/pcss.25.4.801-810.

[22] A. Raghdi, M. Heraiz, M. Rasheed, and A. Keziz, "Investigation of halloysite thermal decomposition through differential thermal analysis (DTA): Mechanism and kinetics assessment," J. Indian Chem. Soc., p. 101413, Oct. 2024, doi: 10.1016/j.jics.2024.101413.

[23] A. Keziz, M. Heraiz, M. Rasheed, and A. Oueslati, "Investigating the dielectric characteristics, electrical conduction mechanisms, morphology, and structural features of mullite via sol-gel synthesis at low temperatures," Mater. Chem. Phys., p. 129757, Jul. 2024, doi: 10.1016/j.matchemphys.2024.129757.

[24] M. Sellam et al., "Improving photocatalytic performance: Creation and assessment of nanostructured SnO2 thin films, pure and with nickel doping, using spray pyrolysis," Ceram. Int., Mar. 2024, doi: 10.1016/j.ceramint.2024.03.094.

[25] S. Moradi et al., "The effect of synthesis parameters on the adsorption capacity of Cu+2 ions of mullite containing polymer composites," J. Aust. Ceram. Soc., Dec. 2024, doi: 10.1007/s41779-024-01125-4.

[26] A. Keziz, M. Rasheed, M. Heraiz, F. Sahnoune, and A. Latif, "Structural, morphological, dielectric properties, impedance spectroscopy and electrical modulus of sintered Al6Si2O13–Mg2Al4Si5O18 composite for electronic applications," Ceram. Int., vol. 49, no. 23, pp. 37423–37434, Dec. 2023, doi: 10.1016/j.ceramint.2023.09.068.

[27] D. Kherifi, A. Keziz, M. Rasheed, and A. Oueslati, "Thermal treatment effects on Algerian natural phosphate bioceramics: A comprehensive analysis," Ceram. Int., May 2024, doi: 10.1016/j.ceramint.2024.05.317.

[28] D. Bouras and M. Rasheed, "Comparison between CrZO and AlZO thin layers and the effect of doping on the lattice properties of zinc oxide," Opt. Quantum Electron., vol. 54, no. 12, Oct. 2022, doi: 10.1007/s11082-022-04161-1.

[29] F. C. Guizellini et al., "Thermal, morphostructural and spectrometric characterization of an antibacterial kaolinite-based filter modified with silver for water treatment," J. Therm. Anal. Calorim., vol. 143, no. 1, pp. 47–60, Jan. 2020, doi: 10.1007/s10973-020-09267-w.

[30] Y. Zeng et al., "Treatment of antibiotics in mariculture wastewater via phosphate-doped porous coralline carbon nitride/porous mullite honeycomb sunlight-driven photocatalytic system: Morphological control, long-term and continuous flow application," Sep. Purif. Technol., vol. 355, p. 129604, Sep. 2024, doi: 10.1016/j.seppur.2024.129604.

[31] N. M. A. Omar et al., "Effect of sintering temperature on functional properties of mullite-kaolinite and stainless steel composed hollow fibre membrane for oil-in-water emulsion separation," J. Taiwan Inst. Chem. Eng., vol. 146, p. 104859, May 2023, doi: 10.1016/j.jtice.2023.104859.